PCCP

Accepted Manuscript

ROYAL SOCIETY OF CHEMISTRY

www.rsc.org/pccp

Origin of colossal permittivity in $(In_{1/2}Nb_{1/2})TiO_2$ via broadband dielectric spectroscopy

Xiao-gang Zhao, Peng Liu*, Yue-Chan Song, An-ping Zhang,

Xiao-ming Chen, Jian-ping Zhou

College of Physics and Information Technology, Shaanxi Normal University, Xi'an, 710062, China

Abstract: $(In_{1/2}Nb_{1/2})TiO_2$ (IN-T) ceramics were prepared via the solid-state reaction route. X-ray diffraction (XRD) and Raman spectroscopy were used for the structural and compositional characterization of the synthesized compound. The results indicated that the sintered ceramic have a single phase of rutile TiO_2. Dielectric spectroscopy (frequency range from 20 Hz to 1 MHz and temperature range from 10 K to 270 K) was performed on those ceramics. IN-T ceramics showed extremely high permittivity up to ~10^3, which can be referred to as colossal permittivity, with relatively low dielectric loss of ~0.05. Most importantly, detailed impedance data analyses of IN-T demonstrated that the electron-pinned defect-dipoles, interfacial and polaron hopping polarizations contribute to the colossal permittivity at high temperatures (270 K); however, only the complexes (pinned electron) and polaron hopping polarization is active at low temperatures (below 180 K), which is consistent with the UDR analysis.

* **Corresponding author:** Tel: +86-029-81530750; fax: +86-029-81530753.
E-mail address: liupeng@snnu.edu.cn (P. Liu).

I. INTRODUCTION

High-performance dielectric materials have been attracting increasing attention because of their applications in myriad types of miniaturized devices and in high-energy-density storage applications.[1,2] With the trend towards size reduction of many microelectronic devices, high-dielectric-constant oxides have become essential for modern microelectronic devices, such as dynamic random access memory (DRAM) devices and on-chip capacitors.

Colossal permittivity (CP) materials, such as doped $BaTiO_3$ perovskites,[3] $CaCu_3Ti_4O_{12}$ (CCTO),[4,5] doped NiO, $La_{2x}Sr_xNiO_4$,[6,7] etc. have been fully accepted as excellent materials for such purposes due to their prodigiously high, temperature independent permittivity. In addition to the broad structural range of these materials, extensive research has been carried out to investigate acceptor and donor dopants to further enhance their dielectric properties.[8-17]

Recently, to further enhance the dielectric permittivity, but with acceptable dielectric loss and less frequency/temperature dependence, the introduction of localized lattice defect states was proposed very recently in work published in Nat. Mater.[18] Hu et al. introduced co-dopants (Nb^{5+} electron-donors, In^{3+} electron-acceptors) into rutile TiO_2, which give rise to the electrons created by both the electron and donors, and the reduction of Ti^{4+} ions is affected by the electron-acceptors in the local lattice defect clusters. Thus, the extraordinary CP ($>10^4$) with low dielectric loss (<0.1) over a wide range of frequency (40 Hz-1 MHz) and temperature (80-450 K) is attributed to the electron-pinned defect-dipoles in this

co-doped TiO_2 material.

In addition, Gai et al. successfully fabricated IN-T films exhibited CP up to 10^4 with low dielectric loss and good frequency stability (up to 10 MHz), which provided a clear evidence for the results of Hu et al.[19] And Cheng et al. introduced co-dopants (Nb^{5+}, Bi^{3+}) into rutile TiO_2, also successfully achieved the CP ($>10^4$) with low dielectric loss (<0.1). Their work is a clear evidence, supporting the CP origin of the electron-pinned defect-dipoles in co-doped TiO_2 system.[20] On the contrary, however, it has been recently argued that the origin of CP is related with the extrinsic IBLC effect rather than the electron-pinned defect-dipoles.[21,22] Li et al. reported that IN-T ceramics present inhomogeneous electrical properties within the grain and grain boundary, leading to IBLC effects and thus CP in the sintered ceramic.

Therefore, there are complex effects on the origin of novel CP performance for co-doped TiO_2 system. In order to clarify those, it is essential to investigate the dielectric properties of IN-T ceramics with broadband dielectric spectroscopy. In this work, $(In_{1/2}Nb_{1/2})TiO_2$ ceramics were prepared using the solid state reaction method, and the dielectric properties were investigated. The results show that the co-doped TiO_2 ceramics with a large dielectric constant up to a few thousand and low loss were obtained at room temperature. Dielectric spectroscopy analysis was performed on IN-T ceramics in order to better understand and investigate the polarization mechanisms associated with colossal permittivity of IN-T ceramic. Here, we found that in addition to the electron-pinned defect-dipoles polarization mechanism and a well-known extrinsic Maxwell-Wagner (MW) polarization, a hopping polaron

mechanism co-exists as an additional polarization mechanism contributes to the colossal permittivity of IN-T ceramics.

II. EXPERIMENTAL

A. Sintering and annealing

The ceramic samples were prepared by the solid-state reaction. Starting materials (TiO_2, In_2O_3, and Nb_2O_5 99.99%) were weighed according to the composition $(In_{1/2}Nb_{1/2})_{0.05}Ti_{0.95}O_2$. The weighed batches were mixed, calcined, and pressed into disks. Finally, the samples were sintered at 1673 K for 10h in Air, and then some samples were annealed at 1273 K for 2h in air.

B. Chemical composition, density, and microstructure

The density of the sintered ceramics was initially measured using the geometrical method and then the Archimedes method for samples showing at least 93% of the theoretical density (4.3 g/cm^3). The ceramic powder morphology and the microstructure of the sintered ceramics were investigated with a field electron gun scanning electron microscope (FEI Nova Nano-SEM 450).

C. X-ray diffraction (XRD) and dielectric property measurements

X-ray diffraction performed on a Rigaku D/max 2250 diffractometer (Japan) with Cu Kα radiation (40 kV and 50 mA). The XRD data for all the samples were measured with a slow scanning speed is 0.01 degree/s. The crystalline phases were also confirmed by using a T64000 Raman spectrometer (Horiba Jobin Yvon S.A.S., France) with an Ar laser (514.5 nm) operated at 50 mW. Prior to electrical

measurements, the sintered ceramic disks were coated with thin gold electrodes (thickness ~30nm) by sputtering (Cressington Scientific Inc., Cressington 108 Auto). The coated samples were placed in a closed cycle cryonic workstation (CFM-9T-H3-IVTI-25 Cryogenic Ltd, London), and dielectric properties as a function of temperature (10 K-270 K) were measured at the different frequencies (20 Hz-1 MHz) through an Agilent 4980a LCR meter. Precision impedance analyzer (Agilent Ltd., Agilent 4980a) combined with cryonic workstation was used in order to perform broadband dielectric spectroscopy analysis (20 Hz-1 MHz) in the temperature range from 10 K to 270 K.

III. RESULTS AND DISCUSSION

A. Microstructure, density, and XRD

The sintered ceramics were dark blue in color due to the reducing sintering atmosphere during high sintering temperature process, but after post-annealed at 1273 K for 2h, the samples post-annealed $(In_{1/2}Nb_{1/2})_{0.05}Ti_{0.95}O_2$ (PA-IN-T) were white yellow in color due to the oxygen atmosphere.[21] The SEM images in Figure 1 shows the microstructures of freshly fractured surfaces of IN-T and PA-IN-T ceramics with a respective average grain size of 86±6 nm and 122±8 nm. Grain sizes were measured by using the mean linear intercept method of ASTM E112 standard.[23] Due to the long time-firing nature of solid state technique, some significant grain growth is observed after sintering and some grain sizes of the sintered ceramics are emerging in the abnormal size comparing to the nearby ones. Density measurement by Archimedes method reveals that the both sintered ceramics have theoretical densities up to 93%

(Table I).

The XRD patterns of the sintered ceramics (0.5% only Nb doped TiO_2 (donated as N-T), 0.5% only In doped TiO_2 (donated as I-T) and 0.5% Nb and In codped TiO_2 (donated as IN-T)) are shown in Figure 2. The XRD patterns are typical of tetragonal rutile crystal structure (PDF 21-1276), and any secondary phase and polymorphs, such as anatase and brookite phases, are not observed for all the samples. To calculate the lattice parameters of IN-T ceramic, Rietveld refinement was performed on the powder XRD data using the software Fullproof and the resulting fit reveals that the IN-T sintered ceramic (Fig. 4(b)) crystallized in a pure rutile structure (PDF:21-1276). Lattice parameters, and theoretical density for the sintered ceramics are summarized in Table I.

Fig. 2(c) shows measured Raman spectra for I-T, N-T, IN-T and pure TiO_2 samples. Four Raman active fundamental modes exist in rutile TiO_2, which can be assigned to B_{1g} (143 cm^{-1}), E_g (447 cm^{-1}), A_{1g} (612 cm^{-1}), and B_{2g} (826 cm^{-1}). B_{1g} and A_{1g} modes are related with O-Ti-O bond bending and Ti-O stretch modes, while the E_g mode is due to out of phase oxygen atom liberation along the c-axis.[24] As shown in Fig. 2c, the B_{1g}, E_g, and A_{1g} modes of pure TiO_2 and of doped TiO_2 ceramics are consistent with the standard modes of pure rutile TiO_2, and this result confirms the rutile phase of the doped ceramics. Note that the peak around 250 cm^{-1} is associated with the second-order Raman scattering in rutile structure.[25,26] Based on the analysis of XRD patterns and Raman spectra, we are convinced that the ceramics doped at moderate levels have a pure rutile phase.

Samples	a(b) (Å)	C (Å)	Grain Size (nm)	Density (%)
IN-T	4.5963	2.9622	86±6	93
AP-IN-T	4.5967	2.9625	122±8	94

B. Dielectric properties and polarization mechanisms

Relative permittivity and dielectric loss of IN-T and PA-IN-T were measured as a function of temperature (10 K-270 K) at different frequencies (20 Hz-1 MHz), and the results are shown in Figure 3. Extremely high permittivity of up to 10^3 with low loss ($\tan\delta \approx 0.05$) is observed at room temperature in both samples. The colossal permittivity of the sintered ceramics decreases in a step-like shape as the temperature decreases, and the relative permittivity becomes independent of temperature below 40 K. This behavior is also found in a well-known high permittivity material CCTO.[27] The decrease of relative permittivity is accompanied by the dielectric loss peak at the given temperature, which indicates a temperature activated dielectric relaxation has occurred: the dielectric loss peaks appear at lower temperatures as frequencies decrease (Figure 3).

Generally, the Debye model can be used to describe the dielectric relaxation, and the relaxation frequency can be represented by

$$v = v_O \exp\left(-\frac{E_A}{k_B T}\right) \quad (1)$$

where v_o, k_B, and E_A represent the pre-exponential factor, the Boltzmann constant, and the activation energy for relaxation, respectively.[28] The imaginary part of the dielectric response (ε″) is proportional to $v\tau/1+(v\tau)^2$, and the maxima of ε″ occurs when $v\tau=1$, where τ is the dielectric relaxation time. Thus, the relaxation temperatures at different frequencies can be extracted from the maximums of ε″ and E_A can be calculated from the Arrhenius plot for Eq. (1).

As such, the ε″ maxima for IN-T and PA-IN-T are determined from Figure 3 and the Arrhenius plots for the both samples are shown in Figure 4. The change in slope of the fitted curves for IN-T samples clearly indicates that three different thermally activated polarization mechanisms exist (Figure 4(a)). By contrast, it is hard to distinguish a slope change at 90-270K for PA-IN-T sample (Figure 4(b)). The activation energies of 0.0208 eV, 0.0195 eV and the jump frequencies of 1.07×10^7 Hz, 2.4×10^7 Hz are obtained for IN-T and PA-IN-T, respectively, in the DR1 region (10 K-80 K), the activation energies of 0.1001 eV, 0.0988 eV and the jump frequencies of 2.3×10^7 Hz, 2.88×10^8 Hz are obtained for IN-T and PA-IN-T, respectively, in the DR2 region (90 K - 180 K), while 0.1536 eV and 1.07×10^9 Hz is calculated in the DR3 region (190 K - 270 K) (Figure 4).

Generally speaking, we believe the doping with In^{3+} demands a positive charge to keep the charge balance, and there should be a negative charge for compensation when the Nb^{5+} occupies the position of Ti^{4+}. As a result, the oxygen vacancies and electrons are generated in order to transfer the charge when In^{3+} and Nb^{5+} substitute

for Ti^{4+}, according to eqn (2) and (3) shown below:

$$In_2O_3 + 2TiO_2 \rightarrow 2In'_{Ti} + V_O^{\cdot\cdot} + 3O_O \quad (2)$$

$$Nb_2O_5 + 2TiO_2 \rightarrow 2Ti'_{Ti} + 2Nb_{Ti}^{\cdot} + 8O_O + \frac{1}{2}O_2 \quad (3)$$

$$Ti^{+4} + e \rightarrow Ti^{+3} \quad (4)$$

Ti^{4+} captures these electrons according to the reaction in eqn (4). In this work, the introduction of Nb^{5+} is considered to be responsible for the reduction of Ti^{4+}, which is prevented, however, when In^{3+} substitutes for Ti^{4+}. The substitution of Nb^{5+} for Ti^{4+} promotes the capture of an electron by Ti^{4+} to form Ti^{3+} in order to keep the charge balance, but the substitution of In^{3+} for Ti^{4+} requires the introduction of a positive charge to surround Ti^{4+} in order to keep the charge balance. As a result, Ti^{4+} still maintains its valence,[19] and this phenomenon can be described by eqn (5):

$$2Ti'_{Ti} + V_O^{\cdot\cdot} \rightarrow TiO_2 \quad (5)$$

It has been widely investigated that long time during high sintering temperature atmosphere of solid state technique can cause high concentration of oxygen vacancies and electrons in the sintered ceramics by eqn (6)[15]

$$O_O \rightarrow \frac{1}{2}O_2 + V_O^{\cdot\cdot} + 2e' \quad (6)$$

Induced oxygen vacancies and electrons can be the localized charge carriers in the grain or at the grain boundary under the applied ac electric field. The origin of colossal permittivity of TiO_2 material system has been recently explained by the interfacial polarization effect by oxygen vacancies in the vicinity of gain boundaries and mobile electrons in the grains.[21,22] However, it is also well known that the

localized charge carriers can induce hopping dipoles in the material by polaron hopping such that these can affect dielectric response of the material.[29,30] Thus, the second polarization mechanism of the colossal permittivity in IN-T could be attributed to a polaron hopping process in the grains. If that is the case, then the large change of activation energies in IN-T compared to AP-IN-T (Figure 4(a)) could be attributed to the higher concentration of polarons due to non-post-annealing of IN-T sample. Right now, we can assumed that the origin of colossal permittivity in IN-T ceramics may due to the contribution of the complexes polarization associated with $In_{Ti}^{'}$, $Nb_{Ti}^{\cdot}$, $Ti_{Ti}^{'}$, $V_O^{\cdot\cdot}$, as well as $In_{Ti}^{'}$- $Nb_{Ti}^{\cdot}$, $In_{Ti}^{'}$-$V_O^{\cdot\cdot}$-$In_{Ti}^{'}$, $In_{Ti}^{'}$-$V_O^{\cdot\cdot}$-$Ti_{Ti}^{'}$, $Nb_{Ti}^{\cdot}$-$Ti_{Ti}^{'}$, $Ti_{Ti}^{'}$-$V_O^{\cdot\cdot}$- $Ti_{Ti}^{'}$, interfacial polarization at the interior insulating grain boundaries, and hopping polarizations in grains by a large number of induced charge carriers. These different contributions to the observed colossal permittivity are schematically depicted in Figure 5.

To further investigate this hypothesis, the universal dielectric response (UDR) model can be applied in order to link conductivity and dielectric response due to localized charge carriers.[31] According to Jonscher's power law, the relative permittivity can be represented as a power law of ω^{s-1} resulting from the Kramers-Kronig transformation for a power law of the ac conductivity, ω^{s}.[31] Therefore, conductivity (σ') and relative permittivity (ε') can be written as

$$\sigma'(f) = \sigma_{dc} + \sigma_0 f^s \quad (7)$$

where σ_{dc} is dc conductivity, σ_o and s represent the temperature dependent constants, and ε_o and f denote the permittivity of free space and experimental frequency (f =

$\omega/2\pi$), respectively. Equation (8) also can be written as

$$f\varepsilon' = A(T)f^{s} \quad (8)$$

where $A(T)= \tan(s\pi/2)\sigma_o\varepsilon_o$ and s is the constant value between 0 and 1. Thus, a straight line should appear in $\log_{10}(\varepsilon_r' f)$ vs. $\log_{10}(f)$ plot at the given temperature, and the slope of the line indicates the value of s.

Figure 6 represents the $\log_{10}(\varepsilon_r' f)$ vs. $\log_{10}(f)$ plot for IN-T at different temperatures (10 K-270 K). A straight line does appear at high temperatures and low frequencies. However, the straight line is deviated from the slope as frequency increases due to relaxation, and consequently it decreases in a step-like shape and forms another straight line at the high frequency region. As temperature decreases, deviations from the slope are gradually occurred at lower frequencies as relaxation frequencies shift to lower frequencies at lower temperature (Figure 6). The values of s are found to be 0.98, 0.97 and 0.95 when obtained from the slopes at 270 K, 60 K and 10 K, respectively. It should be noted that the value of s as closer to "1" indicates polarization charges that are more strictly localized.[32]

In the standard polaron model, the value of s tends to increase and becomes closer to "1" as temperature decreases since the hopping dipoles freeze at low temperatures.[32] Interestingly, however, it is shown here that for the IN-T ceramics, the value of s decreases as temperature decreases, which means charge carriers for polarization are less localized at low temperatures when compared to high temperatures. This indicates that, while hopping polarization and interfacial polarization associated with mobile electrons in the grains and oxygen vacancies at

the vicinity of the grain boundaries are becoming inactive at low temperatures due to insufficient energy to overcome energy barrier for polarization, gathering of the complexes polarization associated with $In_{Ti}^{'}$, $Nb_{Ti}^{\cdot}$, $Ti_{Ti}^{'}$, $V_O^{\cdot\cdot}$, as well as $In_{Ti}^{'}$- $Nb_{Ti}^{\cdot}$, $In_{Ti}^{'}$-$V_O^{\cdot\cdot}$-$In_{Ti}^{'}$, $In_{Ti}^{'}$-$V_O^{\cdot\cdot}$-$Ti_{Ti}^{'}$, $Nb_{Ti}^{\cdot}$-$Ti_{Ti}^{'}$, $Ti_{Ti}^{'}$-$V_O^{\cdot\cdot}$- $Ti_{Ti}^{'}$ are still active as a polarization mechanism. Thus, the higher value of s may be due to the fact that the electrons for complexes polarization are pinned and hardly to move in the grains compared to hopped electrons with oxygen vacancies for hopping polarization and interfacial polarization associated with mobile electrons in the grains and oxygen vacancies at the vicinity of the grain boundaries.

Figure 7 shows the permittivity and dielectric loss change of the IN-T sample as a function of frequency (20 Hz-1 MHz) at different temperatures (10 K-270 K). At high temperatures, three polarization mechanisms (the complexes, space charge and polarons) are able to contribute to the colossal permittivity of IN-T and form the upper plateau (Figure 7). As frequency increases, the permittivity decreases significantly with a correlated dielectric loss peak (Figure 7). This is consistent with dielectric relaxation as described by Debye theory,[27] where relaxation frequencies are also shifted to lower frequencies as temperature decreases.

To further depict this behavior, the relative permittivity and dielectric loss of IN-T between 20 Hz and 1MHz are separately shown in Figure 8 for representative temperatures across the range investigated. It is observed that an extremely high permittivity of up to 2.4×10^3 and dielectric loss below 0.05 are achieved at 300K between 1 KHz and 100 KHz. Here, the colossal permittivity is maintained ($\varepsilon' >10^3$)

up to 100 KHz, however, it drops significantly as frequency increases from 100 kHz to 1MHz, and correspondingly dielectric loss shows sharp increases to tanδ ≈ 0.05 (Figure 8 (c)); this physically meaningless value is rather a clear indication of the onset of conductivity at those higher frequencies.

By contrast, at low temperature, no colossal permittivity is observed and, for example, at 10 K, the highest permittivity is ~105. Moreover, the decrease in relative permittivity as the measuring frequency increases is markedly different when low and high temperature responses are compared. At high temperature (Figure 8 (c)), permittivity, it is clear that the drop in permittivity undergoes three relaxation mechanisms with different characteristic frequencies, while at low temperature, only one relaxation mechanism with very low characteristic frequency is active (Figure 8 (a)). This further confirms that the complexes, interfacial and polaron hopping polarizations contribute to the colossal permittivity at high temperatures (270 K); however, only the complexes (pinned electron) and polaron hopping polarization is active at low temperatures (below 180 K), which is consistent with the UDR analysis.

Furthermore, to gain insight into the physical characteristics of the processes driving these relaxations, it is important to recall that in the thermally activated polaron hopping model, the maximum of the imaginary part of the relative permittivity, ε″, is related to the number of hopping polarons by

$$\varepsilon''_{max} = N\mu^2 / 3k_B T \quad (9)$$

where N and μ represent the number of hopping polarons and the hopping dipole moment, respectively. N is exponentially dependent on the temperature, which can be

written as

$$N = N_0 \exp\left(-E_A / k_B T\right) \tag{10}$$

where N_o is the pre-exponential factor and E_A is the activation energy associated with dielectric relaxation of hopping dipoles.[33,34] Thus, substituting Eq. (10) into Eq. (9) results in

$$T\varepsilon''_{max} = \frac{N_0 \mu^2}{3k_B T} \exp\left(-E_A / k_B T\right) \tag{11}$$

The imaginary part of the relative permittivity for IN-T is plotted in Figure 9 as a function of frequency (20 Hz-1 MHz) between 90 K and 170 K. The ε''_{max} obtained for each temperature was then plotted in the Arrhenius form ($\ln(\varepsilon''_{max}\ T)$ vs. $1/T$) to calculate the activation energy for hopping polarization (Figure 10). It is clear that two linear slopes appear with a transition temperature around 180 K. Accordingly, activation energies of 0.0902 eV and 0.0198 eV are calculated from the fitted line for high (130 K-160 K) and low temperature (80 K-120 K) regions, respectively. Not surprisingly ε''_{max} increases as temperature increases, which further confirms that thermally activated polarization, associated with polaronic dipoles, is a contributing polarization mechanism to the colossal permittivity of IN-T.

More importantly, comparison between the activation energy for the Middle temperature (E_{AM}) and low temperature (E_{AL}) regions can reveal the activation energy for the different polarization mechanisms (similar to the analysis of the data in Figure 4) as follows:

$$E_{AM} = E_{AP} + E_{AE} \tag{12}$$

$$E_{AL} = E_{AE} \tag{13}$$

where E_{AP} and E_{AE} are the activation energies for the hopping polarization and the electron-pinned defect-dipoles polarization in the colossal permittivity of BT, respectively. From Figure 4(a), E_{AM} and E_{AL} were calculated as 0.1100 eV and 0.0198 eV; using these values in Eqs. (12) and (13), E_{AP} of 0.0902eV and E_{AL} of 0.0198 eV are obtained. These results are in good agreement with the calculated activation energy (E_{AE}=0.0195 eV) for high temperature region by using the thermally activated polaronic model (Figure 10).

IV. CONCLUSION

In the current work, $(In_{1/2}Nb_{1/2})TiO_2$ ceramics ceramics were synthesized by the solid-state reaction route. Scanning electron microscopy revealed that sintered ceramics have nanoscale grains. Dielectric measurements demonstrated that sintered ceramics have colossal permittivity up to ~10^3 at room temperature and 1 kHz. This colossal permittivity can be maintained up to 100 kHz at room temperature. Onset of dielectric relaxation following Debye theory occurred as temperature decreased. Activation energy changes for relaxation indicate that at least three different relaxational polarization mechanisms may be contributing the colossal permittivity in $(In_{1/2}Nb_{1/2})TiO_2$. While hopping polarization and interfacial polarization associated with mobile electrons in the grains and oxygen vacancies at the vicinity of the grain boundaries are becoming inactive at low temperatures due to insufficient energy to overcome energy barrier for polarization, gathering of the complexes polarization associated with InTi', NbTi•, TiTi', VO••, as well as InTi'- NbTi•, InTi'-VO••-InTi',

InTi'-VO••-TiTi', NbTi•-TiTi', TiTi'-VO••- TiTi' are still active as a polarization mechanism. According to UDR model, in addition to the gathering of the complexes polarization, the interfacial polarization at insulating grain boundary, and polarization due to polaron hopping was proposed as a co-existing polarization mechanism in the colossal permittivity of $(In_{1/2}Nb_{1/2})TiO_2$ ceramics.

Acknowledgements

This study is supported by the National Natural Science Foundation of China (No. 51372147), the Fundamental Research Funds for the Central Universities (GK201502005, GK201401003), Shaanxi Normal outstanding doctoral dissertation (S2012YB05, X2013YB01), Specialized Research Fund for the Doctoral Program of Higher Education (No. 20120202110004).

Reference

1 C. C. Homes, T. Vogt, S. M. Shapiro, S. Wakimoto and A. P. Ramirez, Science, 2001, 293, 673.

2 S. Krohns, P. Lunkenheimer, S. Meissner, A. Reller, B. Gleich, A. Rathgeber, T. Gaugler, H. U. Buhl, D. C. Sinclair and A. Loidl, Nat. Mater., 2011, 10, 899.

3 M. T. Buscaglia, M. Viviani, V. Buscaglia, L. Mitoseriu, A. Testino, P. Nanni, Z. Zhao, M. Nygren, C. Harnagea,D. Piazza and C. Galassi, Phys. Rev. B: Condens. Matter Mater.Phys., 2006, 73, 064114.

4 M. A. Subramanian, D. Li, N. Duan, B. A. Reisner and A. W. Sleight, J. Solid State Chem., 2000, 151, 323.

5 A. P. Ramirez, M. A. Subramanian, M. Gardel, G. Blumberg, D. Li, T. Vogt and S. M. Shapiro, Solid State Commun., 2000, 115, 217.

6 J. B. Wu, C. W. Nan, Y. H. Lin and Y. Deng, Phys. Rev. Lett., 2002, 89, 217601.

7 S. Krohns, P. Lunkenheimer, C. Kant, A. V. Pronin, H. B. Brom, A. A. Nugroho, M. Diantoro and A. Loidl, Appl. Phys. Lett., 2009, 94, 122903.

8 N. Ikeda, H. Ohsumi, K. Ohwada, K. Ishii, T. Inami, K. Kakurai, Y. Murakami, K. Yoshii, S. Mori, Y. Horibe and H. Kito, Nature, 2005, 436, 1136.

9 C. C. Wang and L. W. Zhang, Appl. Phys. Lett., 2006, 88, 042906.

10 M. Li, A. Feteira, D. C. Sinclair and A. R. West, Appl. Phys. Lett., 2006, 88, 232903.

11 Y. Liu, R. L. Withers and X. Y. Wei, Phys. Rev. B: Condens. Matter Mater. Phys., 2005, 72, 134104.

12 Y. Zhu, J. C. Zheng, L. Wu, A. I. Frenkel, J. Hanson, P. Northrup and W. Ku, Phys. Rev. Lett., 2007, 99, 037602.

13 L. Zhang and Z. J. Tang, Phys. Rev. B: Condens. Matter Mater. Phys., 2004, 70, 174306.

14 S. Krohns, P. Lunkenheimer, S. G. Ebbinghaus and A. Loidl, J. Appl. Phys., 2008, 103, 084107.

15 S. Guillemet-Fritsch, Z. Valdez-Nava, C. Tenailleau, T. Lebey, B. Durand and J. Y. Chane-Ching, Adv. Mater., 2008, 20, 551.

16 P. Lunkenheimer, V. Bobnar, A. V. Pronin, A. I. Ritus, A. A. Volkov and A. Loidl, Phys. Rev. B, 2002, 66, 052105.

17 P. Lunkenheimer, S. Krohns, S. Riegg, S. G. Ebbinghaus, A. Reller and A. Loidl, Eur. Phys. J.: Spec. Top., 2010, 180, 61.

18 W. Hu, Y. Liu, R. L. Withers, T. J. Frankcombe, L. Nor´en, A. Snashall, M. Kitchin, P. Smith, B. Gong, H. Chen, J. Schiemer, F. Brink and J. Wong-Leung, Nat. Mater., 2013, 12, 821.

19 Z. G. Gai, Z. X. Cheng, X. L. Wang, L. L. Zhao, N. Yin, R. Abah, M. L. Zhao, F. Hong, Z. Y. Yua and S. X. Dou, J. Mater. Chem. C, 2014, 2, 6790.

20 X.J. Cheng, Z.W. Li and J.G. Wu, J. Mater. Chem. A, 2015, 3, 5805.

21 J. L. Li, F. Li, Y. Y. Zhuang, L. Jin, L. H. Wang, X. Y. Wei, Z. Xu and S. J. Zhang, J. Appl. Phys., 2014, 116,074105.

22J.L. Li, F. Li, C. Li, G. Yang, Z. Xu and S.J. Zhang, Sci. Rep. 2015, 5.

23 H. Abrams, Metallography, 1971, 4, 59.

24 A. Gajovic, M. Stubicar, M. Ivanda and K. Furic, J. Mol.Struct., 2001, 563, 315-320.

25 C. A. Melendres, A. Narayanasamy, V. A. Maroni and R. W. Siegel, J. Mater. Res., 1989, 4, 1246–1250.

26 V. Swamy, B. C. Muddle and Q. Dai, Appl. Phys. Lett., 2006, 89, 163118.

27 M. A. Subramanian, D. Li, N. Duan, B. A. Reisner, and A. W. Sleight, J. Solid State Chem. 2000, 151, 323.

28 J. R. Macdonald, Impedance Spectroscopy (Wiley, New York,1987).

29 C.C. Wang and L.W. Zhang, New J. Phys. 2007, 9, 210.

30 Y. H. Li, L. Fang, L. J. Liu, Y. M. Huang, and C. Z. Hu, Mater. Sci. Eng. B, 2012 177, 673.

31 A. K. Jonscher, J. Phys. D: Appl. Phys. 1999, 32, R57.

32 A. S. Nowick and B. S. Lim, Phys. Rev. B, 2001, 63, 184115.

33 D. C. Sinclair, T. B. Adams, F. D. Morrison, and A. R. West, Appl. Phys. Lett., 2002, 80, 2153.

34 T. B. Adams, D. C. Sinclair, and A. R. West, Adv. Mater., 2002, 14, 1321.

Figure Captions

FIG. 1. SEM images for (a) IN-T and (b) AP-IN-T sintered ceramics.

FIG. 2. (a) Measured powder XRD data for sintered N-T, I-T and IN-T ceramics. (b) Rietveld refinement results for the sintered IN-T ceramic. The sintered ceramic has rutile crystal structure without any secondary phase. (c) Raman spectra for N-T, I-T and IN-T ceramics compared with pure TiO_2.

FIG. 3. Dielectric property of (a) IN-T and (b) AP-IN-T as a function of temperature (10–270 K).

FIG. 4. Activation energy of thermally activated relaxations for (a) IN-T and (b) AP-IN-T.

FIG. 5. The gathering of the complexes polarization, Interfacial and hopping polarization model for the colossal permittivity of IN-T ceramics.

FIG. 6. The $\log_{10}(\varepsilon'_r f)$ vs. $\log_{10}(f)$ plot for IN-T at different temperatures (10 K-270 K).

FIG. 7. Dielectric properties of IN-T sample as a function of frequency (40 Hz-1 MHz) at different temperatures (10 K-270 K).

FIG. 8. (a)(b)&(c) Frequency dependence of ε of sample IN-T measured from 10 to 270 K with step 10 K. (d)&(e) The Arrhenius plots for the IN-T.

FIG. 9. The imaginary part of the relative permittivity changes for IN-T as a function of frequencies (20 Hz-1 MHz) at 90 K-170 K.

FIG. 10. Activation energy for polaron hopping polarization at 90 K-170 K.

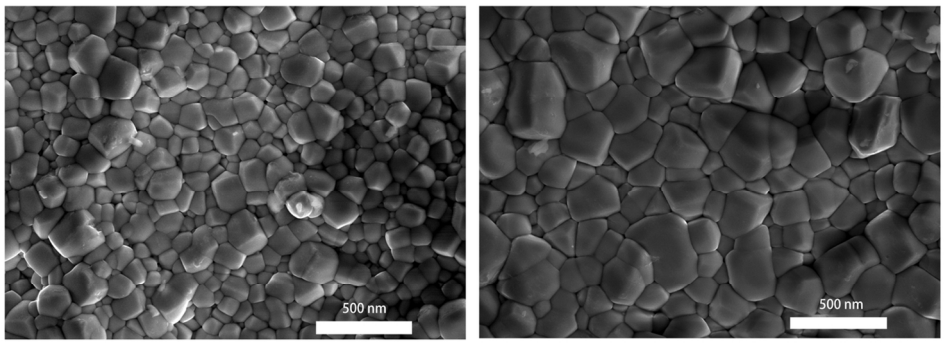

FIG. 1. SEM images for (a) IN-T and (b) AP-IN-T sintered ceramics.
60x22mm (600 x 600 DPI)

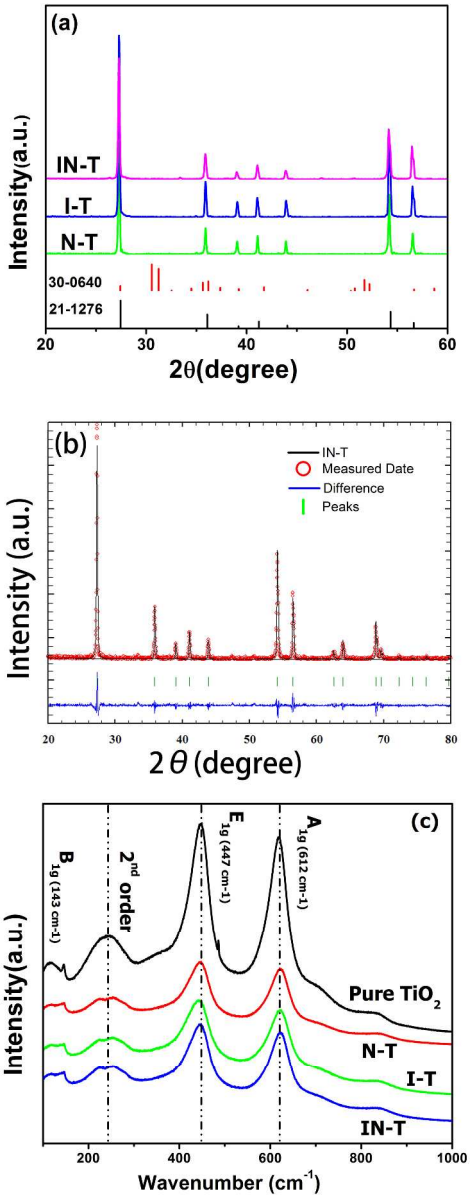

(a) Measured powder XRD data for sintered N-T, I-T and IN-T ceramics. (b) Rietveld refinement results for the sintered IN-T ceramic. The sintered ceramic has rutile crystal structure without any secondary phase. (c) Raman spectra for N-T, I-T and IN-T ceramics compared with pure TiO2.
133x223mm (600 x 600 DPI)

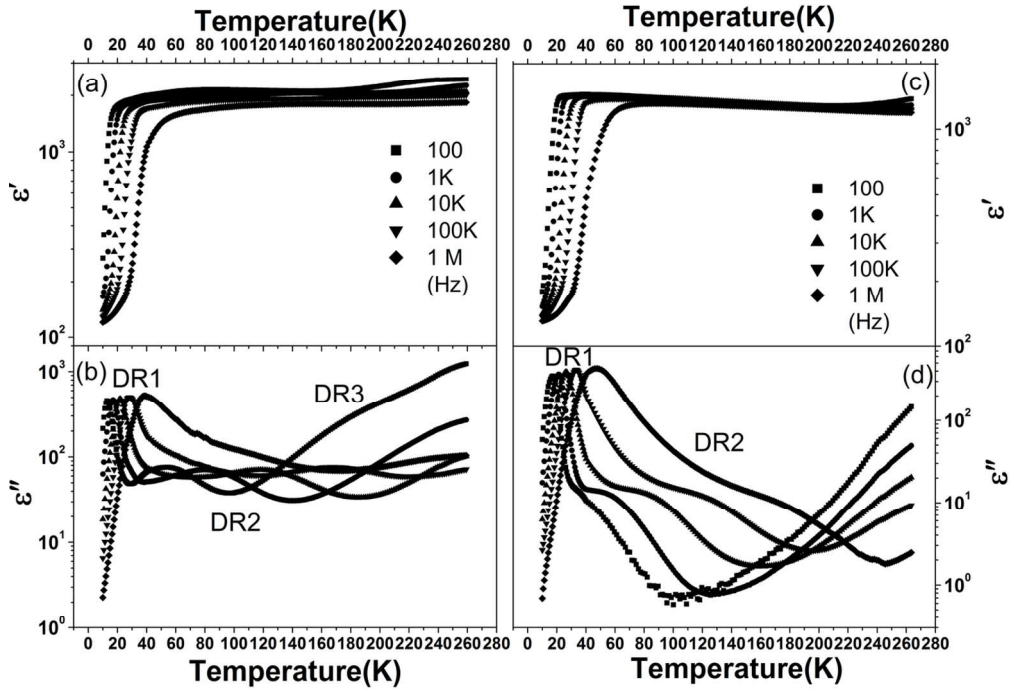

FIG. 3.Dielectric property of (a) IN-T and (b) AP-IN-T as a function of temperature (10–270 K).
60x45mm (600 x 600 DPI)

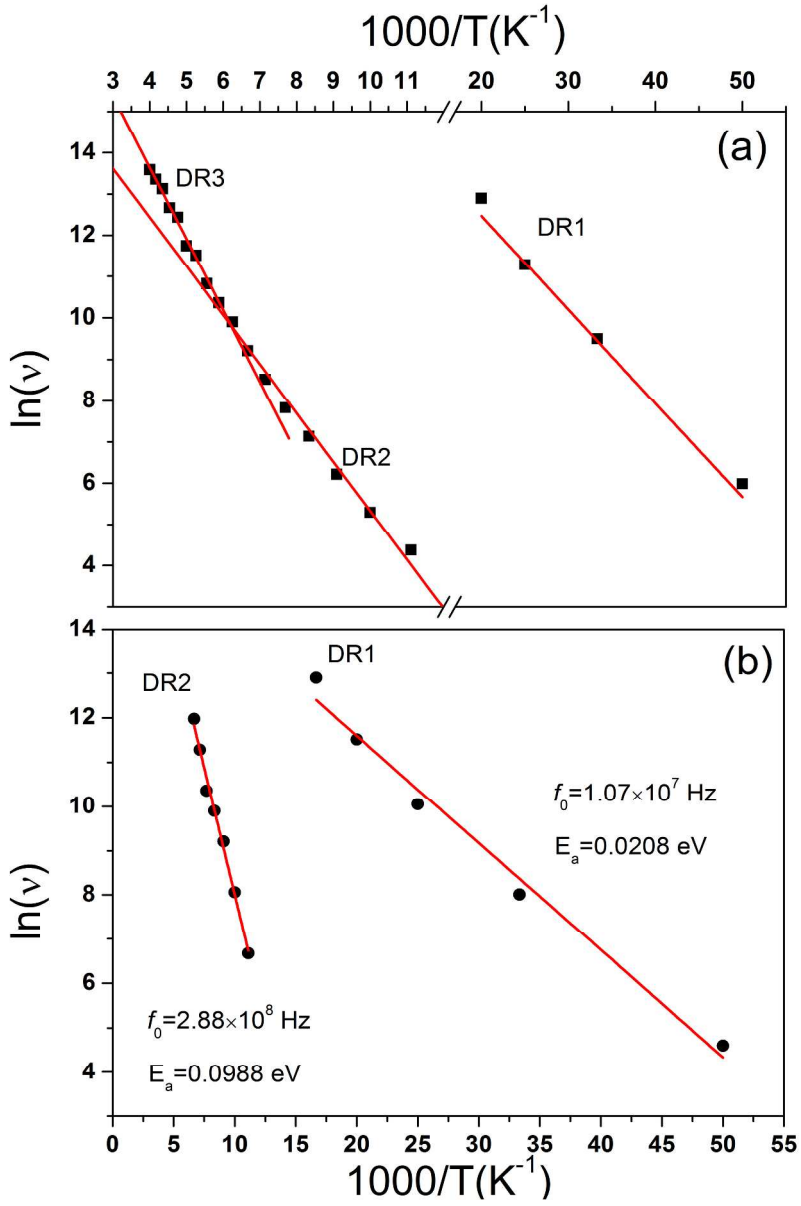

FIG. 4. Activation energy of thermally activated relaxations for (a) IN-T and (b) AP-IN-T.
121x182mm (600 x 600 DPI)

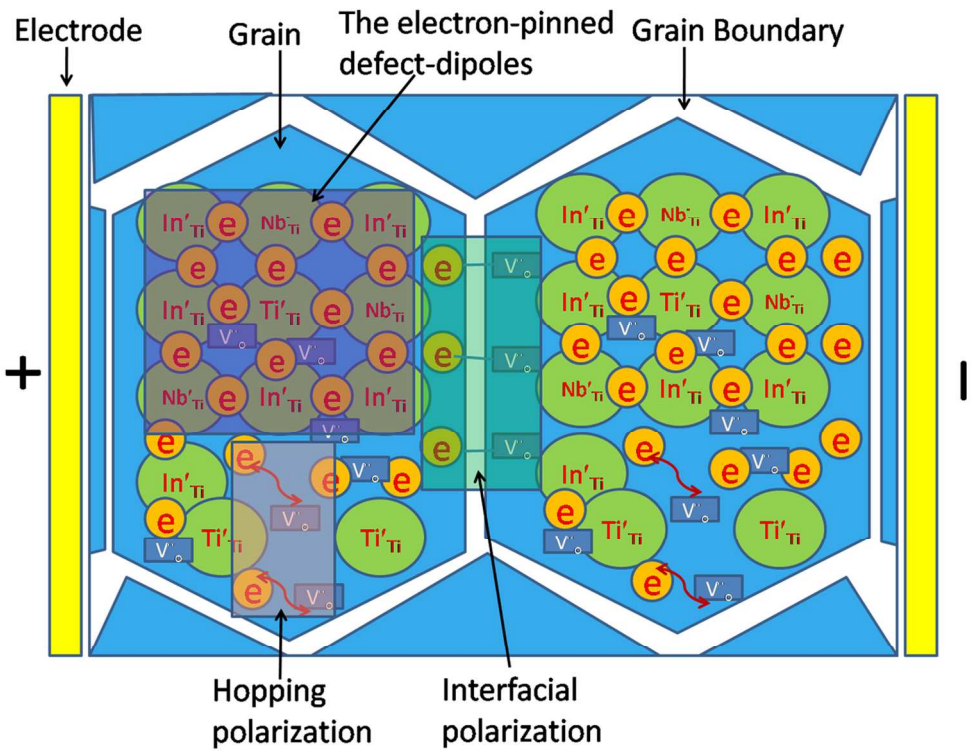

FIG. 5. The gathering of the complexes polarization, Interfacial and hopping polarization model for the colossal permittivity of IN-T ceramics.
60x45mm (600 x 600 DPI)

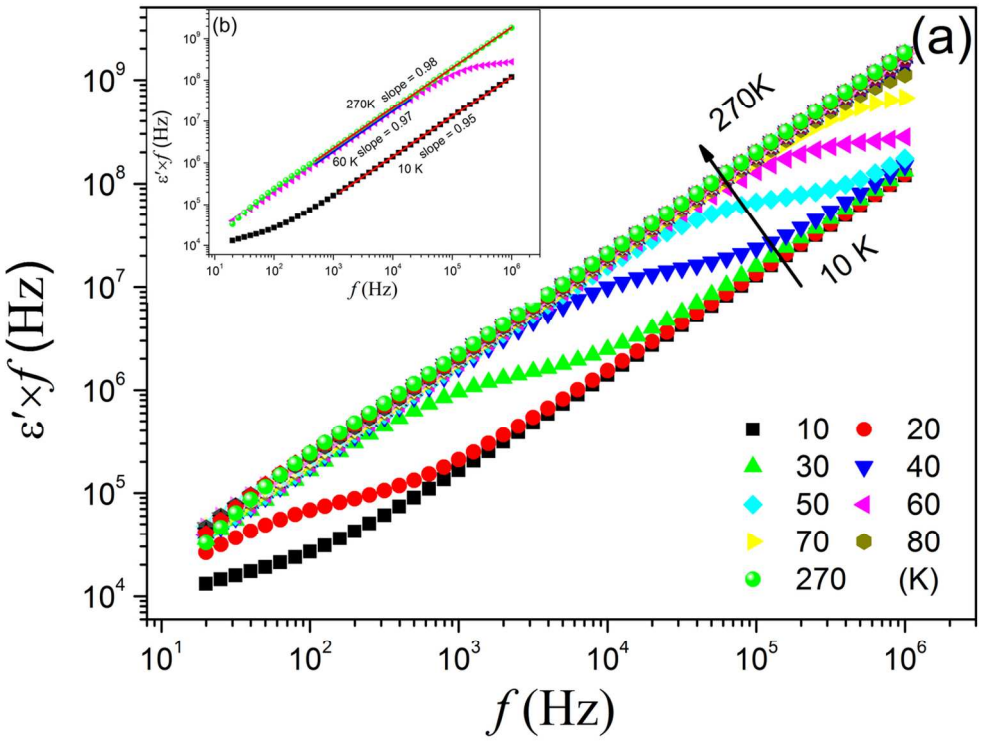

FIG. 6. The log10(ε'rf) vs. log10(f) plot for IN-T at different temperatures (10 K-270 K).
60x45mm (600 x 600 DPI)

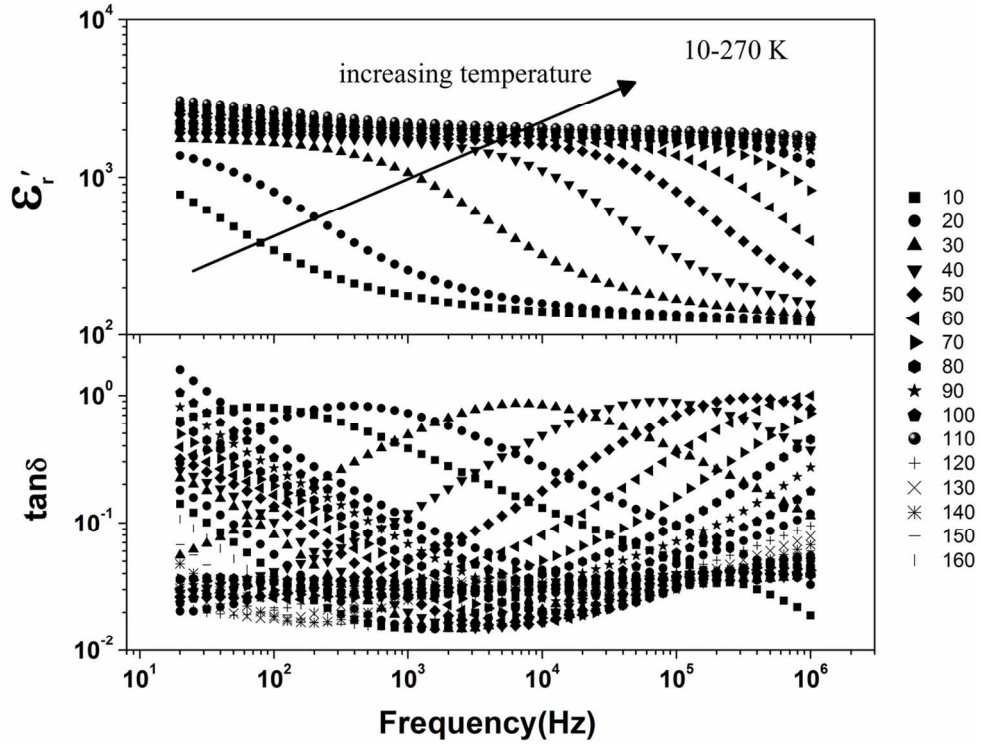

FIG. 7. Dielectric properties of IN-T sample as a function of frequency (40 Hz-1 MHz) at different temperatures (10 K-270 K).
59x44mm (600 x 600 DPI)

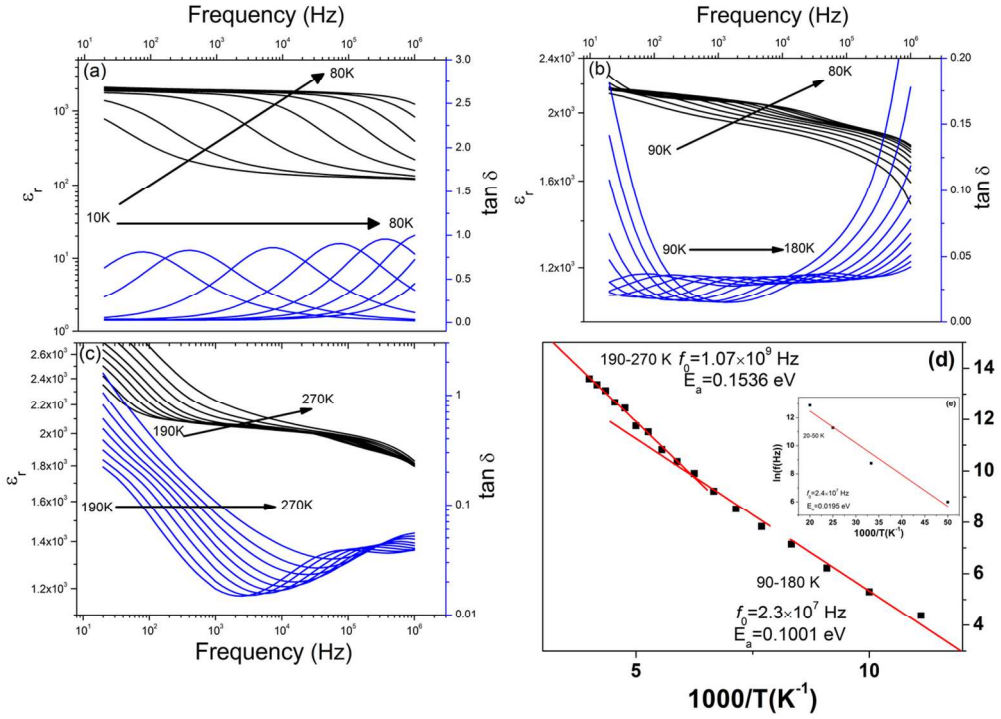

FIG. 8. (a)(b)&(c) Frequency dependence of ε of sample IN-T measured from 10 to 270 K with step 10 K. (d)&(e) The Arrhenius plots for the IN-T.
60x45mm (600 x 600 DPI)

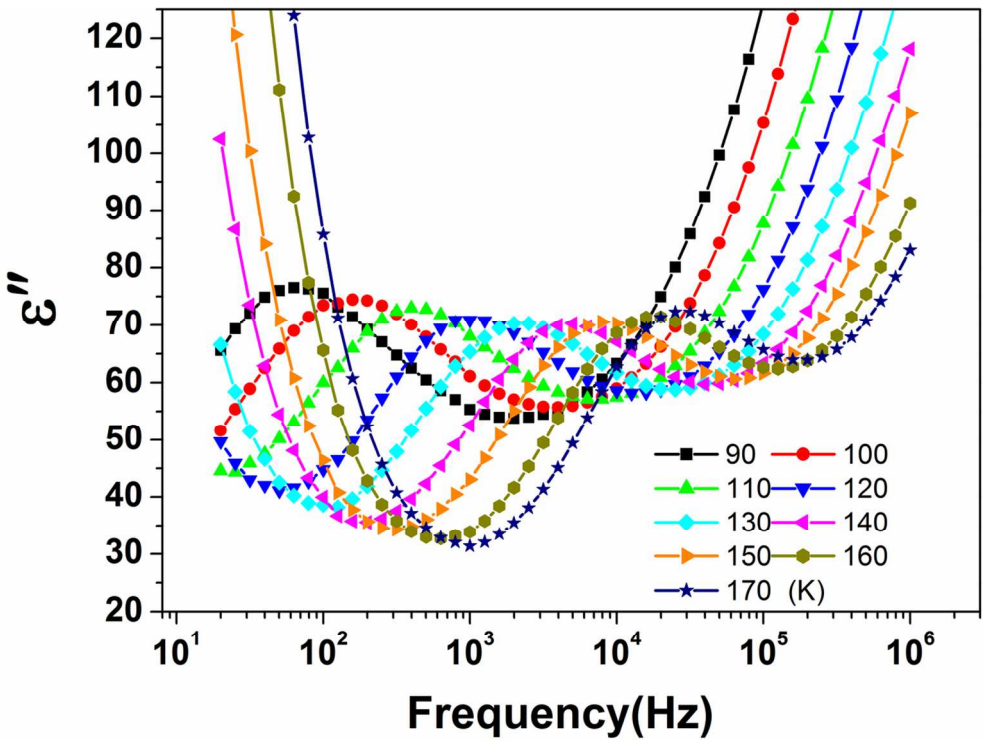

FIG. 9. The imaginary part of the relative permittivity changes for IN-T as a function of frequencies (20 Hz-1 MHz) at 90 K-170 K.
58x42mm (600 x 600 DPI)

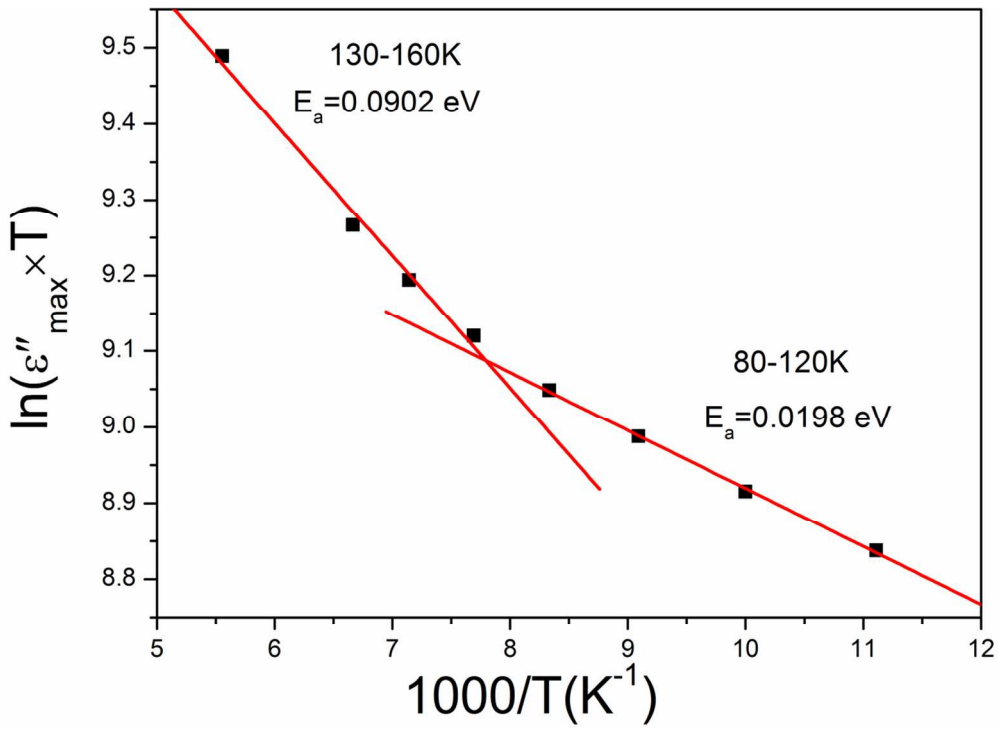

FIG. 10. Activation energy for polaron hopping polarization at 90 K-170 K.
57x41mm (600 x 600 DPI)